Title

Photoinduced Electron Transfer from ZrOCo Binuclear Light Absorber to Pyridine Elucidated by Transient Optical and Infrared Spectroscopy

Journal

The Journal of Physical Chemistry C, 122(35)

ISSN

1932-7447

Authors

Hill, Adam D
Katsoukis, Georgios
Frei, Heinz

Publication Date

2018-09-06

DOI

10.1021/acs.jpcc.8b06435

Peer reviewed

Photo-Induced Electron Transfer from ZrOCo Binuclear Light Absorber to Pyridine Elucidated by Transient Optical and Infrared Spectroscopy

Adam D. Hill[a*], Georgios Katsoukis, and Heinz Frei[*]

Molecular Biophysics and Integrated Bioimaging Division, Lawrence Berkeley National Laboratory, University of California, Berkeley, CA 94720

HMFrei@lbl.gov, AHill@stlawu.edu

(*J. Phys. Chem. C*, accepted)

[a] Permanent address: Department of Chemistry, St. Lawrence University, Canton, NY 13617

Abstract

All-inorganic heterobinculear units can be excited to a metal-to-metal charge transfer (MMCT) state by visible and ultraviolet light, and form the core of multicomponent artificial photosystems that rely on conjugated molecular wires to transmit electrons and holes across ultrathin silica separation membranes to catalytic sites. To understand electron transfer from a heterobinuclear unit to an organic molecule, model systems consisting of pyridine interacting with $Zr^{IV}OCo^{II}$ or $Ti^{IV}OCo^{II}$ sites on silica nanoparticles were assembled and spectroscopically characterized. Transient optical absorption spectroscopy combined with infrared analysis revealed that visible light excitation of assemblies in which pyridine interacts with the Zr center of the ZrOCo unit results in sub-10 nanosecond separation by electron transfer to the organic moiety. Rapid-scan FT-IR spectroscopy supported by density functional theory confirmed the identity of the pyridine radical anion charge-separated state. This state shows a lifetime of 220 (±60) ms prior to complete recovery of the initial state, suggesting spin crossover along the electron transfer path. No hole transfer from excited $Zr^{IV}OCo^{II} \rightarrow Zr^{III}OCo^{III}$ to pyridine is observed. The rectifying charge transfer behavior is an important design aspect for developing efficient artificial photosystems.

1. Introduction

Artificial photosystems offer the potential for providing clean, scalable, renewable energy by transforming atmospheric sources of carbon dioxide and water into energy-dense chemical fuels.[1] Our design for a hybrid molecular/solid-state system uses robust all-inorganic heterobinuclear units composed of two dissimilar metal centers from opposite sides of the transition block: early metals like zirconium, paired with late metals like cobalt, and bridged by an oxo moiety.[2,3] Absorption of visible light creates an excited metal-to-metal charge transfer (MMCT) state between the centers.[4-9] In the case of ZrOCo anchored on a silica surface, the Co donor center is oxidized from Co^{II} to Co^{III} while the Zr acceptor is reduced from Zr^{IV} to Zr^{III}. Coupling of the Zr and Co centers to nanoparticulate CO_2 reduction and H_2O oxidation catalysts, respectively, affords corresponding catalytic transformations[10-14] including the closing of the photosynthetic cycle of converting CO_2 and H_2O to CO and O_2.[13] Understanding charge separation and electron transfer is crucial to the development of an artificial photosystems for sunlight-to-fuel conversion.[15] Yet, kinetics and mechanism of electron transfer from Zr to an acceptor have not been investigated by time-resolved spectroscopy.

Nitrogen-containing conjugated heterocycles are frequently employed as probes to understand the properties of surfaces and reduction/oxidation chemical processes.[16,17] To investigate electron transfer from the binuclear unit to an organic acceptor, we selected pyridine because its redox properties permit electron transfer from transient Zr^{III} of excited ZrOCo units, while hole transfer from transient Co^{III} to pyridine is energetically inaccessible.[18,19] Hence, the redox energetics of ZrOCo light absorber interacting with pyridine allows us to explore MMCT-induced electron transfer to an acceptor molecule by transient spectroscopy (Figure 1). Previous time-resolved optical absorption studies characterized the dynamics of an isolated binuclear light

absorber, $Ti^{IV}OMn^{II}$,[5,6,17] and revealed a long-lived excited MMCT state (microseconds at room temperature) due to a spin state change at the d^1 metal center upon visible light absorption.[20]

Here, we report combined time-resolved UV-visible and FT-IR measurements to characterize the electron transfer from zirconium(III) to pyridine. Using the anchoring method established in earlier work, we have assembled ZrOCo or TiOCo binuclear units on 12 nm sized silica nanoparticles. The spectral profile of the optical ground state bleach and infrared characterization revealed that assemblies of ZrOCo and pyridine in which the organic interacts with the Zr acceptor center produce a long-lived pyridine radical anion species. We show that the electron transfer to the pyridine occurs on the sub-10 ns timescale, with the charge-separated state persisting for hundreds of milliseconds at room temperature before undergoing back electron transfer to ground state, most likely influenced by spin crossover at the transient tetrahedral cobalt(III) center.

2. Experimental Section

2.1. Materials. Compounds were purchased from Sigma-Aldrich and used as received unless otherwise noted. Solvents in Sureseal bottles were opened under inert nitrogen atmosphere for the addition of activated molecular sieves (3 Å for acetonitrile, 4 Å for dichloromethane) and dried for a minimum of 72 hours before use.

2.2 Synthesis. Syntheses of mononuclear Ti, Zr, and Co, and TiOCo and ZrOCo heterobinuclear sites on 12 nm silica nanoparticles were adapted from our previous publications.[4,12,13] Metal ions were loaded at ca. 1 mol% to prevent oxide cluster formation.

Ti-SiO_2np and Zr-SiO_2np (1.0 mol%). Preparation of each compound followed an identical protocol, differing only by the addition of titanocene dichloride or zirconocene dichloride. Briefly, 1.78 g (29.6 mmol) of silica nanopowder (12 nm average diameter) was dried at 200ºC for 2 hours under high vacuum then dispersed in 100 mL dichloromethane with 30 minutes of sonication. Zirconocene (86.6 mg, 0.296 mmol) was also dried under high vacuum and added to the silica suspension in four 10 mL aliquots of dichloromethane. The suspension was sonicated for 10 minutes to fully mix before adding 1.0 mL of triethylamine. The reaction mixture was stirred at 1500 rpm for 17 hours. The particles were collected via vacuum filtration and washed with 100 mL of dichloromethane and transferred to a shallow crucible for calcination, ramping at 5 ºC/min to 550 ºC and holding for 8 hours.

TiOCo-SiO_2np and ZrOCo-SiO_2np (1.0 mol% Zr, 0.9 mol% Co). Ti-SiO_2np or Zr-SiO_2np powder was dehydrated in a high vacuum flask at 200ºC for three hours, then 100 mL of dry acetonitrile was added to 1.52 g (25.3 mmol) of powder and the flask was sonicated for 30 minutes. Anhydrous $CoCl_2$ (Fluka) was further dried at 180ºC for two hours, then added to the nanopowder flask via dissolution in six 8 mL aliquots of acetonitrile. The solution was stirred at 1500 rpm and 1.0 mL of triethylamine was added. After 16 hours, the solution was filtered and vacuum dried, then ground in an agate mortar and pestle. The particles were calcined using a 2ºC/min ramp rate, followed by holding at 350ºC for 8 hours. The resulting ZrOCo-SiO_2nps and TiOCo-SiO_2nps were stored in vials.

Co-SiO_2np (1.0 mol%). Synthesis of cobalt monometallic particles was performed using an identical protocol to the heterobinuclear particles, but beginning from unmodified silica nanopowder.

Pyridine dosing. Powder samples were loaded with pyridine through two protocols. For gas loading, pyridine was degassed by three freeze-thaw cycles at a vacuum line. The resulting pyridine was added to sample pellets in doses of 1 Torr, followed by evacuation to remove loosely bound molecules.

All other samples for the spectroscopic experiments reported here were prepared using a solution-phase loading technique in which 150 mg of nanopowder were suspended in 30 mL of isopropanol or methanol with 15 minutes of sonication, followed by the addition of 7.0 mL of 2.0 mM pyridine in isopropanol or methanol solution. The mixture was further sonicated for 30 minutes to ensure maximum dispersion, then rotovapped to dryness, ground with mortar and pestle, and further dried for 3 hours under vacuum. The dry powders with pyridine, Zr-pyr, Ti-pyr, ZrOCo-pyr, TiOCo-pyr, and Co-pyr, were stored in vials.

2.3. Sample Preparation. Nanopowder samples were pressed into self-supporting pellets with 18 mg of material under 10 tons of force in a 12.7 mm die. Samples for FT-IR and UV-vis transmission spectroscopy were placed in a home-built miniature stainless steel vacuum cell equipped with CaF_2 or KBr windows and evacuated for 2 hours.[21] Pellets for transient absorption spectroscopy were hung from a narrow piece of lab tape at a 45º angle to the perpendicular excitation and probe beam paths in a custom-made quartz cuvette with O-ring vacuum adapter and evacuated for 2 hours. When appropriate, sub-atmospheric pressures of gases were added to either the stainless steel or quartz cells. For XPS studies, pellets were attached to the sample stage with carbon sticky dots and evacuated in the instrument transfer chamber for 4 hours prior to measurements. For FT-Raman, nanopowder was packed into a small depression in an aluminum stub.

2.4. Instrumentation. Samples were characterized using UV-visible, infrared, and X-ray photoelectron spectroscopies. UV-visible spectra of pellets were recorded using a Shimadzu UV-2450 spectrometer. Infrared spectra were measured using a Bruker Vector 33 spectrometer with a liquid-nitrogen-cooled HgCdTe (MCT) detector. Raman spectra were measured using a Bruker IFS66V spectrometer with FRA 106/S FT-Raman module equipped with a 1064 nm Nd:YAG excitation source running at 150 mW and a liquid-nitrogen-cooled Ge detector. X-ray photoelectron spectroscopy was performed using a Kratos Axis Ultra with an aluminum K_α source at 1486.6 eV. Data collection and analysis were performed using CasaXPS software.

Transient absorption spectroscopy (TAS) utilized an Edinburgh Instruments LP920 spectrometer with a pulsed Xe probe lamp. Excitation pulses were provided by a Continuum Surelite II Nd:YAG laser with a Surelite OPO Plus optical parametric oscillator. A low-pass filter in the excitation line was used to remove residual 355 nm light after the OPO. Pulses were 9±1 ns in duration with a 1 Hz repetition rate and energy of 15 mJ/pulse, focused to a spot size on the pellet with a diameter of ca. 5 mm. Monochromator and PMT detector were run in two configurations, depending on type of measurement: For detailed kinetics data, the monochromator slits were opened to produce 10 nm spectral resolution and the detector was set to fast response/high bandwidth. Probing at the short wavelength side of the excitation wavelength avoided background signals caused by sample fluorescence. A high-pass optical filter in front of the monochromator entrance slit removed all light at wavelengths longer than 400 nm, protecting the detector from scattered excitation pulse signal. At these settings, data were obtained by averaging 600 sequences of three shots: pump on, pump off, and probe off. The latter removed the small amount of scattered excitation source background, resulting in higher

sensitivity at short times. For spectral maps, the monochromator slits were narrowed to produce 5 nm of spectral resolution and the detector was set to slow response/low bandwidth mode, and the high pass filter was removed. At these settings, data were the result of averaging 64 pulse sequences at each probe wavelength.

Rapid-scan FT-IR (RS-FT-IR) spectroscopy was performed using a Bruker model Vertex 80V instrument equipped with a liquid-nitrogen-cooled MCT detector (Kolmar Technologies KMPV8-1-J2 with an 8 μm bandgap). For photolysis, an Excelsior 405C-200-CDRH 200 mW continuous-wave laser source emitting at 405 nm was used. A quartz prism was used to align the excitation laser beam in a collinear geometry with the infrared probe beam and a long focal length lens allowed expansion of the beam to 12 mm diameter in order to fully cover the pellet. Sample pellets were placed in the infrared vacuum cell with an additional 10 mg SBA-15 mesoporous silica pellet behind them to ensure complete scattering of the visible laser light for protection of the infrared detector element. Light pulses were generated by intercepting the laser beam with a mechanical shutter with variable opening times (Vincent Associates model Uniblitz controlled by a BNC pulse generator model 565). For precise synchronization of excitation pulse and spectra data acquisition, opening of the shutter was triggered by the forward motion of the FT-IR interferometer mirror. The measurement protocol consisted of recording an interferogram during a 120 ms excitation pulse followed by nine interferograms of 120 ms duration during the subsequent dark period. Data were the average of 200 such sequences. The spectral resolution was 4 cm^{-1}.

2.5. Data Analysis and Computational Modeling. Data averaging, fitting, and plotting were performed using scripts written in python 3.5.2 through the Enthrough Canopy IDE (v.2.1.9)

with the *lmfit* package (v.0.9.2.9) for non-linear least squares fitting.[22] Density functional theory (DFT) geometric optimization and frequency calculations for neutral and radical pyridine species were performed using Q-Chem 4.3 running on an IBM System x3850 high-performance computer.[23-27] The density functionals B3LYP, BP86, and ωB97X-D were used with 6-31G*, 6-31++G**, and aug-cc-pVDZ basis sets.[28-30] Due to the well-known shortcomings of DFT in computing electron transfer processes (electrons tend to be overly delocalized) and electronic transitions (time-dependent DFT is necessary to find transition probabilities), modeling complete binuclear units with organics on silica surfaces is beyond the scope of this work.[31,32]

3. Results

3.1 Spectroscopic Characterization

X-ray photoelectron spectroscopy was used to quantify the concentration of anchored heterobinuclear units, as summarized in Table S1. Relative sensitivity factors were applied to convert integrated peak areas into relative elemental abundances.[33] Typical metal/Si atom ratios were 1% for the early metal (Ti or Zr) and 0.4-0.8% for cobalt, which in previous work was found to result in samples free of undesired polynuclear clusters featuring more than two metal centers. The slight excess of Ti or Zr ensured that a minimum of isolated Co centers were formed.[34] XPS measurements in the presence of pyridine were not feasible because of the considerable vapor pressure (4.8 Torr at 273 K).

UV-visible absorption spectra of ZrOCo and TiOCo anchored on SiO_2np, and those of the corresponding monometallic samples are in good agreement with results of previous work (Figure 2).[4,12-14] In the earlier studies, these binuclear units were anchored in the channels of

mesoporous silica MCM-41 or SBA-15, which are highly visible-light-scattering materials that require optical spectroscopy in diffuse reflectance mode. By contrast, pressed wafers of silica nanoparticles scatter much less in the visible region and are suitable for conducting measurements in transmission mode; residual light scattering can be removed by computer subtraction. Monometallic Ti and Zr do not possess any optical absorption in the visible up to 330 nm where the onset of the O-Ti LMCT transition of tetrahedral Ti^{IV} occurs.[4] For Co containing samples shown in Figure 2 traces (a), (b), and (c), the three spin orbit peaks near 515, 590, and 650 nm of tetrahedral Co^{II} d-d ligand field transition are seen. Absorption by the continuous MMCT transition of TiOCo (trace (a)) and ZrOCo (trace (b)) samples overlaps with the Co^{II} d-d band and continues to increase towards the UV region.[4,12-14] The absence of polynuclear clusters beyond ZrOCo or TiOCo units, i.e. Co oxide, titanate or zirconia clusters, was confirmed by FT-Raman spectroscopy in the 800-200 cm^{-1} region where such clusters feature sharp intense bands (Figure S1).[10,34] As shown in the inset of Figure 2, adding pyridine results in minor shifts of the peaks of the Co d-d transition as a result of interaction of Co with pyridine. The latter is more distinctly manifested in the infrared spectrum, discussed next. Pyridine does not possess optical absorption at wavelengths longer than 300 nm; the lowest energy transition has a peak at 256 nm.[35]

FT-IR spectra at frequencies above the intense asymmetric Si-O stretch absorption of silica that blocks observation between 1300 and 1000 cm^{-1} reveal distinct bands of adsorbed pyridine for the various metal functionalized surfaces, as shown in Figure 3 and summarized in Table S2. Adsorption of pyridine was conducted either from the gas phase or by solution loading, in the latter case using methanol or isopropanol as solvent. Because gas phase loading resulted in spectra featuring molecules interacting with metal centers as well as residual non-

interacting pyridine on the silica surface even after prolonged evacuation (Figure S2) while solution loading gave exclusively metal bound pyridine, only results obtained by solution loading using methanol are presented here. Among the infrared bands of pyridine adsorbed on metal-free silica nanoparticles (Figure 3a) with peaks at 1379, 1390, 1448, 1460, 1470, 1491, 1547, 1600, 1632, 1638 cm^{-1}, the bands below 1600 cm^{-1}, which are mainly C-H deformation modes, exhibit very small shifts of 1 to max. 3 cm^{-1} for monometallic Ti-SiO_2np (Figure 3b) and Zr-SiO_2np (trace c). By contrast, the 1600 cm^{-1} ν(CC,CN) stretch mode shifts to higher frequencies by 9 cm^{-1} for both the Ti and the Zr sample. Similarly significant shifts are observed for the ring stretch modes at 1632 and 1638 cm^{-1}, which increase for Ti to 1640 and 1654 cm^{-1}, and to 1640 and 1660 cm^{-1} in the case of Zr. Hence, the ring stretch bands in the 1600-1700 cm^{-1} window indicate interaction of pyridine with the group IVB metal center; accompanying intensity changes compared to pyridine adsorbed on metal-free silica are minor. By contrast, both absolute and relative infrared band intensities of pyridine adsorbed onto monometallic Co-SiO_2np under identical loading conditions differ substantially from those of Ti and Zr-SiO_2np. Specifically, Co-SiO_2np bands shown in Figure 3d at 1451, 1611, and 1655 cm^{-1} are 3 to 5 times more intense than the corresponding peaks of pyridine adsorbed on Ti or Zr-SiO_2 nanoparticles, which implies significantly stronger interaction of pyridine with Co than with a group IVB metal center. Notable differences between pyridine on Co-SiO_2np compared with Zr-SiO_2np are a peak intensity ratio of 1451/1491 cm^{-1} of 7:1 for Co-SiO_2np compared to approximately 1:1 for 1448/1491 cm^{-1} in the case of Zr, and a fairly intense 1470 cm^{-1} band of Zr-SiO_2np that is barely visible in the case of the Co sample. Furthermore, the overtone mode at 1655 cm^{-1} for the Co sample shifts to 1660 cm^{-1} for Zr-SiO_2np. Another difference is a small band at 1548 cm^{-1} in the Zr-SiO_2np sample, also present in plain SiO_2 and Ti-SiO_2, that is either absent or barely visible in

Co-SiO_2np and the binuclear samples. This absorption is most likely due to pyridinium formed by residual Broensted acid sites in plain silica [36] or in the presence of Zr or Ti, but practically absent in Co containing SiO_2 samples.

Infrared spectra of heterobinuclear TiOCo and ZrOCo silica nanoparticles shown in Figure 3e and 3f, respectively, represent in good approximation a superposition of the spectra of the corresponding monometallic samples. The remarkably close agreement of the observed ZrOCo-SiO_2np spectrum (Figure 3f) with the computed superposition of the Zr (trace (c)) and Co (trace (d)) spectra (no scaling) is shown in Figure 4. This result strongly suggests that the distribution of pyridine upon adsorption onto ZrOCo groups reflects the relative strength of interaction with each type of metal. There is no indication in the spectra for the presence of significant amounts of pyridine molecules that do not interact with one of the metal centers. We conclude that, based on infrared intensities, approx. 20% of pyridine molecules interact with Zr or Ti and 80% with Co.

3.2 Transient Optical Absorption Spectroscopy

Wafers of ZrOCo-SiO_2np loaded with pyridine (infrared spectrum shown in Figure 3f) were excited into the broad ZrOCo MMCT absorption with 9 ns laser pulses at wavelengths starting at the high energy end of the Co^{II} d-d band at 500 nm and tuning towards shorter blue wavelengths. The lowest excitation energy at which transient signals appeared was 425 nm, with the result shown in Figure 5. A transient peak appears at 375 nm accompanied by a bleach at 412 nm. The shape indicates strongly overlapping decreasing ground state and increasing excited state absorption bands that exhibit almost no decay on the hundreds of μs time scale. As will be described below, accompanying FT-IR experiments revealed a lifetime of 220 ms. At the same

time, a decrease of the characteristic Co^{II} d-d ground state absorption between 500 and 650 nm is noted (inset of Figure 5).[37,38] When exciting ZrOCo SiO_2np wafers without adsorbed pyridine at the same wavelength, no transient absorption features are detected on the tens of μs and longer time scale (Figure S3a). These observations indicate that pyridine directly participates in a photophysical process initiated by $Zr^{IV}OCo^{II} \rightarrow Zr^{III}OCo^{III}$ excitation. By contrast, no signal was detected for pyridine-loaded TiOCo SiO_2np (Figure S3c). Hence, the less reducing Ti acceptor (compared to Zr) of excited TiOCo MMCT units is not sufficiently energetic to initiate the process. As expected, no transient was encountered for pyridine loaded onto monometallic Co-SiO_2np samples (Figure S3b), pellets with pyridine on bare silica, or on monometallic Ti- or Zr-grafted silica.

Spectral deconvolution of the overlapping bands using peak fitting revealed a bleach centered at 408 nm with FWHM of 55 nm, which is strongly overlapped by growth of a similarly broad band centered at 403 nm (FWHM of 65 nm), as shown in Figure S4. The bands were described by pseudo-Voigt profile (approximating the convolution of Lorentzian homogeneous broadening and Gaussian inhomogeneous broadening, with the latter dominating). It is important to note that the strong overlap of the decreasing and increasing bands means that the positive and negative peak intensities are highly correlated, resulting in substantial uncertainty regarding band intensities. However, the effect on the center frequencies of the peaks for fits with large variation of band intensity is negligible.

Interestingly, no transient signal was observed upon excitation at modestly longer excitation wavelength of 437 nm, as evident from Figure S3d. This observation is consistent with the shape of the bleach of the ground state absorption (Figure S4) according to which 437 nm light excites just the tail end of the transition. We conclude that the ground state absorption

initiating the observed photochemical process is substantially narrower than the ZrOCo MMCT absorption.

The temporal behavior of the transient absorption maximum at 375 nm and bleach at 400 nm of pyridine loaded ZrOCo SiO_2np is shown in Figure 6, trace (a) and (c), respectively. The rise time $\tau = 9\pm1$ ns is limited by the 9 ns laser pulse width, as expected for a MMCT initiated process featuring optical electron transfer from Co^{II} donor. Also shown in Figure 6 trace (b) is the behavior of absorbance at 375 nm for the pyridine loaded TiOCo sample, which merely represents the residual electrostriction effect caused by light absorption by the MMCT chromophore (see Sect. 2) as described in previous work.[6]

To examine the possible role of quenching by gaseous oxygen, ZrOCo-SiO_2np wafers were exposed to varying pressures of O_2 up to 800 Torr during transient optical measurements. No effect on the transient signal shown in Figure 5 was noted.

3.3 Rapid-Scan FT-IR Spectroscopy

The very small decay of the transient optical signal even over hundreds of microseconds indicates that the lifetime of the state generated by excitation with a 425 nm laser pulse extends to the time scale of milliseconds and possibly beyond. Hence, monitoring of the photo-induced process by rapid-scan FT-IR spectroscopy to obtain structural information of the transients involved may be explored. For time-resolved FT-IR experiments, loading of pyridine at 0.5 mol % (relative to Si) was found most practical, which is approximately two times higher than for the samples described in Figure 5. The corresponding infrared spectrum of pyridine loaded ZrOCo-SiO_2np wafers is presented in Figure 7a.

Figure 7b shows rapid-scan spectra in the 1700-1300 cm^{-1} region with the initial time slice recorded during the 120 ms laser excitation pulse (405 nm, close to the maximum of the ground state bleach), and the following 8 slices during the subsequent dark period measured 60, 180, 300, 420, 540, 660, 780, 900 ms (midpoints) after termination of the excitation pulse (the last slice at 1080 ms was used for background subtraction). As can be seen in Figure 7b, the observed transient bands disappeared completely prior to arrival of the next laser excitation pulse, which allowed us to average the result of 200 light on/off cycles for signal-to-noise improvement.

A cursory inspection of the time resolved FT-IR spectra, Figure 7b, reveals bleaching of all pyridine absorptions and growth of sharp (positive) bands, some partially overlapped by decreasing pyridine modes. DFT calculations were employed to guide identification of the transient generated; gas-phase structures of pyridine using the ωB97X-D density functional produced accurate matches to pyridine and related transient species. As shown for the complete set of pyridine vibrations presented in Table S8, five normal modes are expected to fall in the 1700-1300 cm^{-1} region (modes number 18-22). According to calculated frequencies of gas-phase pyridine radical anion and cation species presented in Table 1, all radical anion and the majority of the cation frequencies of this spectral region show red shifts relative to the corresponding mode of pyridine. Frequency shifts to lower values are expected for radical ions due to increased occupancy of antibonding or reduced occupancy of bonding orbitals. Clearly, the agreement between observed product bands and computed anion frequencies is substantially closer than for the modes calculated for the cation species. Specifically, the product peak of the ν_{20} mode at 1445 cm^{-1} overlaps with the bleach of ν_{19} of pyridine at 1440 cm^{-1}, thereby diminishing its apparent intensity. The product peak for ν_{21} (1484 cm^{-1}) is red shifted by 170 cm^{-1} with respect to

the bleach for pyridine ν_{21} mode at 1653 cm^{-1}. The agreement of DFT calculated frequencies with those observed for pyridine and pyridine radical anion is close for all modes except ν_{19} for which the discrepancy is tens of cm^{-1} for both species. Overall, the match between the pattern of the DFT calculated frequencies for the anion and those of the growing bands is satisfactory. Therefore, we identify the transient species as pyridine radical anion. No transient infrared bands other than those assigned to pyridine radical anion were observed. Furthermore, spectra recorded after photochemical runs did not indicate accumulation of any products, which is consistent with a reversible photophysical process (Figure S6).

Analogous rapid-scan FT-IR experiments with pyridine-loaded TiOCo-SiO_2np samples did not reveal any transient signals above the noise level, as shown in Figure 7c (the small band around 1625 cm^{-1} is due to the presence of residual H_2O).

For quantifying the kinetics of back electron transfer of the pyridine radical anion, integrated intensities of the 1630 cm^{-1} product band were used together with those of the 1653 and 1667 cm^{-1} pyridine absorptions. As shown in Figure 8, agreement within uncertainties was found for the single exponential decay of the radical anion species, 220 ± 60 ms, and the recovery of pyridine, 280 ± 60 ms.

4. Discussion

The combined observations of transient optical and infrared spectroscopy reveal photo-induced electron transfer from the ZrOCo unit to pyridine adsorbed on the silica nanoparticle surface. The transient bleach of the Co^{II} d-d band (Figure 5 inset) directly manifests the role of Co^{II} as electron donor, and the absence of the electron transfer to pyridine upon excitation of TiOCo

units confirms that the MMCT chromophore of ZrOCo is responsible for the light triggered process. Regarding the latter observation, while the MMCT absorption of $TiOCo^{II}$ is stronger than that of $ZrOCo^{II}$ at any visible wavelength, transient Ti^{III} falls short by at least 0.5 eV of the reduction potential needed for electron transfer to pyridine.

The 403 nm maximum of the transient absorption is in agreement with literature reports according to which the π-π^* transition of pyridine radical anion between 300 and 400 nm is shifted towards the long wavelength end of this range when interacting with electron rich, large metal centers such as Zr.[38-45] Furthermore, the ratio of 20:1 for the observed peak intensity of the 403 nm growth and the 500-650 nm bleach (Figure 5) agrees reasonably well with reported extinction coefficients of pyridine radical anion of 2000 L mol^{-1} cm^{-1} and overlapping tetrahedral Co^{II} d-d (200 L mol^{-1} cm^{-1}) and Co^{III} d-d (50 L mol^{-1} cm^{-1}).[47,48] A conceivable alternative charge transfer process, namely hole transfer from transient Co^{III} to pyridine, is ruled out by the observed simultaneous growth of the 403 nm intermediate and the bleach of Co^{II}. The absence of hole transfer to pyridine is to be expected because pyridine is known to be exceptionally resistant to one-electron oxidation.[49] Further evidence that pyridine radical cation is not formed is provided by the infrared results. Gas phase pyridine radical cations dissociate readily to HCN and 1,3-butadiene cation radical,[50-53] which would readily be visible by FT-IR monitoring; no characteristic infrared band of a cyano group is detected. Furthermore, the infrared spectrum of the transient does not agree with the pyridine radical cation modes calculated by DFT (Table 1). We conclude that, based on time resolved optical and infrared spectroscopic evidence, visible light induces $pyr–Zr^{IV}–O–Co^{II} \rightarrow pyr^{\bullet -}–Zr^{IV}–O–Co^{III}$ electron transfer between the MMCT unit and adsorbed pyridine.

Two striking findings are the much narrower than expected spectral width of the ground state MMCT bleach in the visible spectrum, and a very slow $pyr^{\bullet-}$–Zr^{IV}–O–Co^{III} → pyr–Zr^{IV}–O–Co^{II} back electron transfer. Comparison of the hundreds of nm wide $Zr^{IV}OCo^{II}$ → $Zr^{III}OCo^{III}$ MMCT absorption across most of the visible spectrum shown in Figure 2 (also in previous publications)[12,13] with the tens of nm wide 408 nm ground state bleach of Figure 5 (Figure S4) indicates that only excitation of a subset of ZrOCo units results in long lived $pyr^{\bullet-}$–Zr^{IV}–O–Co^{III} states. We propose that the subset of sites leading to long lived charge separation between ZrOCo and pyridine consists of the ones for which pyridine interacts with the Zr center of the binuclear unit, identified by FT-IR spectroscopy in Figure 3. The general acid-base interaction of the Zr center with adjacent pyridine may involve some degree of electron donation to the metal. Even modest electron delocalization in the ground state would result in direct photoexcitation of a pyr–Zr^{III}–O–Co^{III} MMCT state with partial $pyr^{\bullet-}$–Zr^{IV}–O–Co^{III} electronic character, opening an efficient path to full charge separation. The broad MMCT absorption at wavelengths outside the 408 nm band originates from ZrOCo units interacting with pyridine at the Co end, as well as ZrOCo sites that lack a pyridine nearest neighbor. No charge (hole) transfer can occur in the former case because pyridine radical cation is not energetically accessible. Hence, for these sites, the only accessible process is Zr^{III}–O–Co^{III} → Zr^{IV}–O–Co^{II} back electron transfer. We conclude that weak electronic coupling of the Zr acceptor center of the binuclear light absorber with pyridine enables electron transfer from the excited MMCT state to pyridine, outcompeting back-electron transfer within the ZrOCo unit.

The origin of the unexpected long lifetime of the charge-separated $pyr^{\bullet-}$–Zr^{IV}–O–Co^{III} state is most likely crossing to a spin forbidden state.[54,55] Our earlier study of TiOMn centers explored spin crossover in binuclear units; we proposed that the transient d^1 metal center was the

most likely site of the spin crossover because it is the conserved feature of a variety of different metal combinations with long-lifetime MMCT states.[20] In ZrOCo-pyr, there is no obvious barrier that would require the electron to remain at the zirconium center to undergo spin crossover before reducing the pyridine; as the spin-orbit coupling of cobalt is higher than pyridine, spin crossover at cobalt is considered more likely.[55-57] Cobalt is known to undergo spin crossover on the ultrafast timescale in a variety of oxidation states, geometries, and phases,[54,56-62] including in our previous works with organometallic systems.[63,64] In particular, this phenomenon has been characterized in great detail in photo-induced magnetization due to metal-to-metal charge transfer states in Prussian blue analogs.[58,65-69] As in those analogs, Co^{III} is commonly found in an octahedral configuration,[57] taking on a tetrahedral geometry when required by ligand steric constraints, as in the tungsten oxide matrices discussed earlier,[48] or with ligands like benzene dithiolates.[70,71] Tetrahedral cobalt centers are most frequently high-spin, and but display a low-spin ground state with strong-field norbornyl or phosphanido ligands.[72,73] Based on this information, we propose that the long lifetime of the $pyr^{\bullet-}$–Zr^{IV}–O–Co^{III} state is the result of spin crossover from the original optically formed quartet state to a doublet state. Our tetrahedral Co^{III} forms in the high-spin state (S = 1) alongside Zr^{III} (S = 1/2). The latter electron is transferred to pyridine and Co^{III} undergoes spin crossover to S = 0. The hundred-millisecond lifetime of this state is long for molecular systems but consistent with solid-state cases where spin-state trapping can be indefinite (Figure 1).[65]

This explanation of the relationship between cobalt(II), zirconium(IV), and pyridine is consistent with experimental descriptions of molecular charge transfer polyads.[74] In cases where the bridging moiety only provides structural connections, the excitation directly from donor to acceptor is detectable and the system is functionally a dyad.[75,76] In cases where coupling between

donor and both bridge and acceptor are strong, excitations to both states are detectable.[77] In cases where the bridge represents an accessible state and direct coupling between donor and acceptor is weak, the evidence of transfer was enhancement in transient signal from the acceptor species (e.g. fluorescence or transient absorption).[78-80] Spectra suggest that our system functions most closely according to this latter type, Co→Zr→pyr. FT-IR spectra reveal two types of ZrOCo sites, namely those with pyridine interacting with the Co center and sites that feature pyridine interacting with the Zr center. Transient optical spectra indicate that only the latter sites undergo electron transfer to pyridine. The donor Co center does not interact directly with the acceptor pyridine. Rather, the Zr-pyridine Lewis acid/base ground state interaction provides weak electronic coupling that, upon excitation of the $Zr^{III}OCo^{III}$ MMCT state, results in efficient transfer of an electron to pyridine. The charge-separated $pyr^{\bullet-}$–Zr^{IV}–O–Co^{III} state so formed gains its hundred-millisecond lifetime by virtue of the effects of spin crossover and the triad-type structure of the pyridine/binuclear assembly.

5. Conclusions

Visible-light-induced electron transfer from excited ZrOCo light absorber to pyridine adsorbed on silica nanoparticle surfaces has been monitored by time-resolved optical and FT-IR spectroscopy. Transfer occurs within the 9 ns instrument response time. Transient pyridine radical anion was identified by optical absorption centered at 403 nm and observation of several infrared ring stretch and CH deformation modes in the 1700-1300 cm^{-1} region whose spectral assignment is supported by DFT calculations. Charge transfer from the MMCT unit to pyridine is manifested by transient depletion of the Co donor d-d absorption. The optical MMCT bleach

of ZrOCo units participating in photo-induced electron transfer to pyridine is substantially narrower than the hundreds of nanometer wide ZrOCo absorption. This finding suggests that a subset of binuclear units engaged in acid-base interaction of the Zr center of ZrOCo units with pyridine, identified by a distinct infrared spectroscopic signature, results in long lived charge separation. The slow back electron transfer of 250 ms at room temperature suggests spin crossover of the charge-separated state at the tetrahedral Co^{III} center.

The discovery of specific interactions of a binuclear MMCT light absorber with heteroaromatic molecules that give rise to visible light induced electron transfer resulting in extremely long lived charge separation provides guidance for designing efficient electron transfer pathways for integrated artificial photosystems. In particular, the finding will guide designs of electronic coupling of heterobinuclear light absorbers to organic wire molecules embedded in ultrathin silica separation membranes, which play a critical role in nanoscale photosynthetic units for CO_2 reduction by H_2O.[81]

Supporting Information

The Supporting Information is available free of charge on the ACS Publications website at DOI: Tables summarizing XPS elemental abundances and infrared frequencies, FT-IR and FT-Raman characterization, TAS and RS-FT-IR control experiments, methods of peak fitting, xyz coordinates and normal modes of DFT-calculated structures of pyridine (PDF).

Acknowledgment

This work was supported by the Director, Office of Science, Office of Basic Energy Sciences, Division of Chemical, Geological and Biosciences of the U.S. Department of Energy under

Contract No. DE-AC02-05CH11231. G.K. gratefully acknowledges the scholarship support from the German Research Foundation (DFG, agreement KA 4403/1-1). A.D.H. acknowledges St. Lawrence University's William B. Bradbury, Jr. Faculty Support Award and thanks Brendan Abolins for helpful discussions on DFT. The authors thank Eran Edri for assistance with XPS experiments.

References

[1] Montoya, J. H.; Seitz, L. C.; Chakthranont, P.; Vojvodic, A.; Jaramillo, T. F.; Nørskov, J. K. Materials for Solar Fuels and Chemicals. *Nat. Mater.* **2016**, *16*, 70.

[2] Lin, W.; Frei, H. Anchored Metal-to-Metal Charge-Transfer Chromophores in a Mesoporous Silicate Sieve for Visible-Light Activation of Titanium Centers. *J. Phys. Chem. B* **2005**, *109*, 4929-4935.

[3] Kim, W.; Edri, E.; Frei, H. Hierarchical Inorganic Assemblies for Artificial Photosynthesis. *Acc. Chem. Res.* **2016**, *49*, 1634-1645.

[4] Han, H.; Frei, H. Visible Light Absorption of Binuclear $TiOCo^{II}$ Charge-Transfer Unit Assembled in Mesoporous Silica. *Microporous Mesoporous Mater.* **2007**, *105*, 265-272.

[5] Wu, X.; Weare, W. W.; Frei, H. Binuclear TiOMn Charge-Transfer Chromophore in Mesoporous Silica. *Dalton Trans.* **2009**, 10114-10121.

[6] Cuk, T.; Weare, W. W.; Frei, H. Unusually Long Lifetime of Excited Charge-Transfer State of All-Inorganic Binuclear $TiOMn^{II}$ Unit Anchored on Silica Nanopore Surface. *J. Phys. Chem. C* **2010**, *114*, 9167-9172.

[7] Blasse, G.; Dirksen, G. J. The Coloration of Titanates by Divalent Metal Ions with a View to Solar Energy Applications. *Chem. Phys. Lett.* **1981**, *77*, 9-11.

[8] Sherman, D. M. Molecular Orbital (SCF-Xα-SW) Theory of Metal-Metal Charge Transfer Processes in Minerals. *Phys. Chem. Miner.* **1987**, *14*, 364-367.

[9] Blasse, G. Optical Electron Transfer Between Metal Ions and its Consequences. *Struct. Bonding* **1991**, *76*, 153-187.

[10] Lin, W.; Frei, H. Photochemical CO_2 Splitting by Metal-to-Metal Charge-Transfer Excitation in Mesoporous ZrCu(I)-MCM-41 Silicate Sieve. *J. Am. Chem. Soc.* **2005**, *127*, 1610-1611.

[11] Han, H.; Frei, H. In Situ Spectroscopy of Water Oxidation at Ir Oxide Nanoclusters Driven by Visbile TiOCr Charge-Transfer Chromophore in Mesoporous Silica. *J. Phys. Chem. C* **2008**, *112*, 16156-16159.

[12] Macnaughtan, M. L.; Soo, H. S.; Frei, H. Binuclear ZrOCo Metal-to-Metal Charge-Transfer Unit in Mesoporous Silica for Light-Driven CO_2 Reduction to CO and Formate. *J. Phys. Chem. C* **2014**, *118*, 7874-7885.

[13] Kim, W.; Yuan, G.; McClure, B. A.; Frei, H. Light Induced Carbon Dioxide Reduction by Water at Binuclear $ZrOCo^{II}$ Unit Coupled to Ir Oxide Nanocluster Catalyst. *J. Am. Chem. Soc.* **2014**, *136*, 11034-11042.

[14] Kim, W.; Frei, H. Directed Assembly of Cuprous Oxide Nanocatalyst for CO_2 Reduction Coupled to Heterobinuclear $ZrOCo^{II}$ Light Absorber in Mesoporous Silica. *ACS Catal.* **2015**, *5*, 5627-5635.

[15] Gust, D.; Moore, T. A.; Moore, A. L. Solar Fuels Via Artificial Photosynthesis. *Acc. Chem. Res.* **2009**, *42*, 1890-1898.

[16] Bird, C. L.; Kuhn, A. T. Electrochemistry of the Viologens. *Chem. Soc. Rev.* **1981**, *10*, 49-82.

[17] Thomas, J. K. Physical Aspects of Photochemistry and Radiation Chemistry of Molecules Adsorbed on Silica, Gamma.-Alumina, Zeolites, and Clays. *Chem. Rev.* **1993**, *93*, 301-320.

[18] Wardman, P. Reduction Potentials of One-Electron Couples Involving Free Radicals in Aqueous Solution. *J. Phys. Chem. Ref. Data* **1989**, *18*, 1637-1755.

[19] Gerke, R. H. A Summary of Electrode Potentials. *Chem. Rev.* **1925**, *1*, 377-395.

[20] McClure, B. A.; Frei, H. Excited State Electron Transfer of All-Inorganic Heterobinuclear $TiOMn^{2+}$ Chromophore Anchored on Silica Nanoparticle Surface. *J. Phys. Chem. C* **2014**, *118*, 11601-11611.

[21] Blatter, F.; Frei, H. Selective Photooxidation of Small Alkenes by O_2 with Red Light in Zeolite Y. *J. Am. Chem. Soc.* **1994**, *116*, 1812-1820.

[22] Newville, M.; Stensitzki, T.; Allen, D. B.; Ingargiola, A. LMFIT: Non-Linear Least-Square Minimization and Curve-Fitting for Python. *Zenodo* **2014**, 11813. http://doi.org/10.5281/zenodo.11813

[23] Shao, Y.; Gan, Z.; Epifanovsky, E.; Gilbert, A. T. B.; Wormit, M.; Kussmann, J.; Lange, A. W.; Behn, A.; Deng, J.; Feng, X., et al. Advances in Molecular Quantum Chemistry Contained in the Q-Chem 4 Program Package. *Mol. Phys.* **2015**, *113*, 184-215.

[24] Porezag, D.; Pederson, M. R. Infrared Intensities and Raman-Scattering Activities within Density-Functional Theory. *Phys. Rev. B* **1996**, *54*, 7830-7836.

[25] Jones, G. S.; Mavrikakis, M.; Barteau, M. A.; Vohs, J. M. First Synthesis, Experimental and Theoretical Vibrational Spectra of an Oxametallacycle on a Metal Surface. *J. Am. Chem. Soc.* **1998**, *120*, 3196-3204.

[26] Fuente, E.; Menéndez, J. A.; Díez, M. A.; Suárez, D.; Montes-Morán, M. A. Infrared Spectroscopy of Carbon Materials: A Quantum Chemical Study of Model Compounds. *J. Phys. Chem. B* **2003**, *107*, 6350-6359.

[27] Zvereva, E. E.; Shagidullin, A. R.; Katsyuba, S. A. Ab Initio and DFT Predictions of Infrared Intensities and Raman Activities. *J. Phys. Chem. A* **2011**, *115*, 63-69.

[28] Feller, D. The Role of Databases in Support of Computational Chemistry Calculations. *J. Comp. Chem.* **1996**, *17*, 1571-1586.

[29] Rassolov, V. A.; Pople, J. A.; Ratner, M. A.; Windus, T. L. 6-31G* Basis Set for Atoms K through Zn. *J. Chem. Phys.* **1998**, *109*, 1223-1229.

[30] Rassolov, V. A.; Ratner, M. A.; Pople, J. A.; Redfern, P. C.; Curtiss, L. A. 6-31G* Basis Set for Third-Row Atoms. *J. Comp. Chem.* **2001**, *22*, 976-984.

[31] Choing, S. N.; Francis, A. J.; Clendenning, G.; Schuurman, M. S.; Sommer, R. D.; Tamblyn, I.; Weare, W. W.; Cuk, T. Long-Lived LMCT in a d^0 Vanadium(V) Complex by Internal Conversion to a State of $3d_{xy}$ Character. *J. Phys. Chem. C* **2015**, *119*, 17029-17038.

[32] Gabrielsson, A.; Matousek, P.; Towrie, M.; Hartl, F.; Zalis, S.; Vlcek, A. J. Excited States of Nitro-Polypyridine Metal Complexes and Their Ultrafast Decay. Time-Resolved IR Absorption, Spectroelectrochemistry, and TD-DFT Calculations of Fac-[Re(Cl)$(CO)_3$(5-Nitro-1,10-Phenanthroline)]. *J. Phys. Chem. A* **2005**, *109*, 6147-6153.

[33] De Groot, F. High-Resolution X-Ray Emission and X-Ray Absorption Spectroscopy. *Chem. Rev.* **2001**, *101*, 1779-1808.

[34] Han, H.; Frei, H. Controlled Assembly of Hetero-binuclear Sites on Mesoporous Silica: Visible Light Charge-Transfer Units with Selectable Redox Properties. *J. Phys. Chem. C* **2008**, *112*, 8391-8399.

[35] Hughes, E. B.; Jellinek, H. H. G.; Ambrose, B. A. Pyridine. Ultraviolet Absorption Spectrum and Dissociation Constant. *J. Phys. Colloid Chem.* **1949**, *53*, 410-414.

[36] Connell, G.; Dumesic, J. A. The Generation of Broensted and Lewis Acid Sites on the Surface of Silica by Addition of Dopant Cations. *J. Catal.* **1987**, *105*, 285-298.

[37] Savitzky, A.; Golay, M. J. E. Smoothing and Differentiation of Data by Simplified Least Squares Procedures. *Anal. Chem.* **1964**, *36*, 1627-1639.

[38] Bromba, M. U. A.; Ziegler, H. Application Hints for Savitzky-Golay Digital Smoothing Filters. *Anal. Chem.* **1981**, *53*, 1583-1586.

[39] Kalyanaraman, V.; Rao, C. N. R.; George, M. V. Radical Anions of Pyridine Derivatives. *J. Chem. Soc. B: Phys. Org.* **1971**, 2406-2409.

[40] Connell, G.; Dumesic, J. A. Acidic Properties of Binary Oxide Catalysts: I. Mössbauer Spectroscopy and Pyridine Adsorption for Iron Supported on Silica. *J. Catal.* **1986**, *101*, 103-113.

[41] Andersson, M. P.; Uvdal, P. Transformation of Pyridine to A-Pyridyl on W(110) as Probed by Vibrational Spectroscopy: Experiments and Calculations. *J. Phys. Chem. B* **2001**, *105*, 9458-9462.

[42] Wu, D.-Y.; Ren, B.; Jiang, Y.-X.; Xu, X.; Tian, Z.-Q. Density Functional Study and Normal-Mode Analysis of the Bindings and Vibrational Frequency Shifts of the Pyridine–M (M = Cu, Ag, Au, Cu^+, Ag^+, Au^+, and Pt) Complexes. *J. Phys. Chem. A* **2002**, *106*, 9042-9052.

[43] Zakrzewski, J.; Delaire, J. A.; Daniel, C.; Cote-Bruand, I. $W(CO)_5$-Pyridine-Acceptor Complexes: Theoretical Calculations and a Laser Photolysis Study. *New J. Chem.* **2004**, *28*, 1514-1519.

[44] Martins, J. B. L.; Fialho, T. A. S. Interaction of Pyridine on Nb_2O_5. *J. Mol. Struct.: THEOCHEM* **2005**, *732*, 1-5.

[45] Suffren, Y.; Rollet, F.-G.; Levasseur-Grenon, O.; Reber, C. Ligand-Centered Vibrational Modes as a Probe of Molecular and Electronic Structure: Raman Spectroscopy of Cis-Fe(1,10-Phenanthroline)$_2$(NCS)$_2$ and Trans-Fe(Pyridine)$_4$(NCS)$_2$ at Variable Temperature and Pressure. *Polyhedron* **2013**, *52*, 1081-1089.

[46] Matz, D. L.; Schalnat, M. C.; Pemberton, J. E. Reaction of Thin Films of Solid-State Benzene and Pyridine with Calcium. *J. Am. Chem. Soc.* **2012**, *134*, 12989-12997.

[47] Dodd, J. W.; Hopton, F. J.; Hush, N. S. The Electronic Spectra of Azabenzene Anions. *Proc. Chem. Soc.* **1962**, 61-62.

[48] Kojima, K.; Matsuda, J. Absorption Spectra of Tetrahedral Co(III) and Co(II) Complexes in Heteropolytungstates. *Bull. Chem. Soc. Jpn.* **1985**, *58*, 821-825.

[49] Turner, W. R.; Elving, P. J. Electrooxidation in Pyridine at Pyrolytic Graphite Electrode. *Anal. Chem.* **1965**, *37*, 467-469.

[50] Zahradník, R.; Čársky, P.; Slanina, Z. Conjugated Radicals. XVIII. Photoelectron Spectroscopy as a Source of Electronic Spectral Data for Radical Cations. *Collect. Czech. Chem. Commun.* **1973**, *38*, 1886-1898.

[51] Eland, J. H. D.; Berkowitz, J.; Schulte, H.; Frey, R. Rates of Unimolecular Pyridine Ion Decay and the Heat of Formation of $C_4H_4^+$. *Int. J. Mass Spectrom. Ion Phys.* **1978**, *28*, 297-311.

[52] Bondybey, V. E.; English, J. H.; Shiley, R. H. Pyridine Radical Cation and Its Fluorine Substituted Derivatives. *J. Chem. Phys.* **1982**, *77*, 4826-4831.

[53] LaVerne, J. A.; Carmichael, I.; Araos, M. S. Radical Production in the Radiolysis of Liquid Pyridine. *J. Phys. Chem. A* **2005**, *109*, 461-465.

[54] Zhang, W.; Gaffney, K. J. Mechanistic Studies of Photoinduced Spin Crossover and Electron Transfer in Inorganic Complexes. *Acc. Chem. Res.* **2015**, *48*, 1140-1148.

[55] El-Sayed, M. A. Spin—Orbit Coupling and the Radiationless Processes in Nitrogen Heterocyclics. *J. Chem. Phys.* **1963**, *38*, 2834-2838.

[56] Fink, K.; Wang, C.; Staemmler, V. Superexchange and Spin–Orbit Coupling in Chlorine-Bridged Binuclear Cobalt(II) Complexes. *Inorg. Chem.* **1999**, *38*, 3847-3856.

[57] Mortensen, S. R.; Kepp, K. P. Spin Propensities of Octahedral Complexes from Density Functional Theory. *J. Phys. Chem. A* **2015**, *119*, 4041-4050.

[58] Kabir, M.; Van Vliet, K. J. Reversible Mechanism for Spin Crossover in Transition-Metal Cyanides. *Phys. Rev. B* **2012**, *85*, 054431.

[59] Biasin, E. et al. Femtosecond X-Ray Scattering Study of Ultrafast Photoinduced Structural Dynamics in Solvated $[Co(terpy)_2]^{2+}$. *Phys. Rev. Lett.* **2016**, *117*, 013002.

[60] Lomont, J. P.; Harris, C. B. Primary Photochemical Dynamics of Metal Carbonyl Dimers and Clusters in Solution: Insights into the Results of Metal–Metal Bond Cleavage from Ultrafast Spectroscopic Studies. *Inorg. Chim. Acta* **2015**, *424*, 38-50.

[61] Rupp, F.; Chevalier, K.; Graf, M.; Schmitz, M.; Kelm, H.; Gruen, A.; Zimmer, M.; Gerhards, M.; van Wuellen, C.; Krueger, H. J., et al. Spectroscopic, Structural, and Kinetic Investigation of the Ultrafast Spin Crossover in an Unusual Cobalt(II) Semiquinonate Radical Complex. *Chem. Eur. J.* **2017**, *23*, 2119-2132.

[62] Yoshimura, A.; Torieda, H.; Ohno, T. Doublet−Quartet Intersystem Crossing and Electron Transfer of Cobalt(II) Moieties in $[LRu^{III}(L–L)Co^{III}]^{5+}$ (L = 2,2‘:6‘,2‘‘-Terpyridine and L–L = a Bridging Ligand). *J. Phys. Chem. A* **2004**, *108*, 2149-2154.

[63] Lomont, J. P.; Nguyen, S. C.; Schlegel, J. P.; Zoerb, M. C.; Hill, A. D.; Harris, C. B. Ultrafast Observation of a Solvent Dependent Spin State Equilibrium in CpCo(CO). *J. Am. Chem. Soc.* **2012**, *134*, 3120-3126.

[64] Lomont, J. P.; Nguyen, S. C.; Zoerb, M. C.; Hill, A. D.; Schlegel, J. P.; Harris, C. B. Observation of a Short-Lived Triplet Precursor in CpCo(CO)-Catalyzed Alkyne Cyclotrimerization. *Organometallics* **2012**, *31*, 3582-3587.

[65] Sato, O.; Iyoda, T.; Fujishima, A.; Hashimoto, K. Photoinduced Magnetization of a Cobalt-Iron Cyanide. *Science* **1996**, *272*, 704.

[66] Sato, O.; Einaga, Y.; Fujishima, A.; Hashimoto, K. Photoinduced Long-Range Magnetic Ordering of a Cobalt−Iron Cyanide. *Inorg. Chem.* **1999**, *38*, 4405-4412.

[67] Cartier dit Moulin, C.; Villain, F.; Bleuzen, A.; Arrio, M. A.; Sainctavit, P.; Lomenech, C; Escax, V.; Baudelet, F.; Dartyge, E.; Gallet, J. J., *et al.* Photoinduced Ferrimagnetic Systems in Prussian Blue Analogues $C^{I}_{x}Co_4[Fe(CN)_6]_y$ (C^{I} = Alkali Cation). 2. X-Ray Absorption Spectroscopy of the Metastable State. *J. Am. Chem. Soc.* **2000**, *122*, 6653-6658.

[68] Escax, V.; Bleuzen, A.; Cartier dit Moulin, C.; Villain, F.; Goujon, A.; Varret, F.; Verdaguer, M. Photoinduced Ferrimagnetic Systems in Prussian Blue Analogues $C^{I}_{x}Co_4[Fe(CN)_6]_y$ (C^{I} = Alkali Cation). 3. Control of the Photo- and Thermally Induced Electron Transfer by the $[Fe(CN)_6]$ Vacancies in Cesium Derivatives. *J. Am. Chem. Soc.* **2001**, *123*, 12536-12543.

[69] Sato, O.; Tao, J.; Zhang, Y. Z. Control of Magnetic Properties through External Stimuli. *Angew. Chem. Int. Ed.* **2007**, *46*, 2152-2187.

[70] Eisenberg, R.; Dori, Z.; Gray, H. B.; Ibers, J. A. Crystal and Molecular Structure of the High-Spin Squar-Planar Complex Triphenylmethylarsonium Bis(Toluene-3,4-Dithiolato)Cobaltate.0.5ethanol. *Inorg. Chem.* **1968**, *7*, 741-748.

[71] Baker-Hawkes, M. J.; Billig, E.; Gray, H. B. Characterization and Electronic Structures of Metal Complexes Containing Benzene-1,2-Dithiolate and Related Ligands. *J. Am. Chem. Soc.* **1966**, *88*, 4870-4875.

[72] Byrne, E. K.; Theopold, K. H. Redox Chemistry of Tetrakis(1-Norbornyl)Cobalt. Synthesis and Characterization of a Cobalt(V) Alkyl and Self-Exchange Rate of a Co(III)/Co(IV) Couple. *J. Am. Chem. Soc.* **1987**, *109*, 1282-1283.

[73] Coburger, P.; Demeshko, S.; Rödl, C.; Hey-Hawkins, E.; Wolf, R. Oxidative P–P Bond Addition to Cobalt(−I): Formation of a Low-Spin Cobalt(III) Phosphanido Complex. *Angew. Chem. Int. Ed.* **2017**, *56*, 15871-15875.

[74] Gust, D.; Moore, T. A. Mimicking Photosynthesis. *Science* **1989**, *244*, 35-41.

[75] Roberts, J. A.; Kirby, J. P.; Wall, S. T.; Nocera, D. G. Electron Transfer within Ruthenium(II) Polypyridyl-(Salt Bridge)-Dimethylaniline Acceptor-Donor Complexes. *Inorg. Chim. Acta* **1997**, *263*, 395-405.

[76] Hsu, T.-L. C.; Engebretson, D. S.; Helvoigt, S. A.; Nocera, D. G. Charge Transfer Photochemistry of Quadruply Bonded Ditungsten Halophosphine Complexes. *Inorg. Chim. Acta* **1995**, *240*, 551-557.

[77] D'Alessandro, D. M.; Keene, F. R. Intervalence Charge Transfer (IVCT) in Trinuclear and Tetranuclear Complexes of Iron, Ruthenium, and Osmium. *Chem. Rev.* **2006**, *106*, 2270-2298.

[78] Willkomm, J.; Orchard, K. L.; Reynal, A.; Pastor, E.; Durrant, J. R.; Reisner, E. Dye-Sensitised Semiconductors Modified with Molecular Catalysts for Light-Driven H_2 Production. *Chem. Soc. Rev.* **2016**, *45*, 9-23.

[79] Antoniuk-Pablant, A.; Kodis, G.; Moore, A. L.; Moore, T. A.; Gust, D. Photoinduced Electron and Energy Transfer in a Molecular Triad Featuring a Fullerene Redox Mediator. *J. Phys. Chem. B* **2016**, *120*, 6687-6697.

[80] Feskov, S. V.; Ivanov, A. I. Effect of Geometrical Parameters of Dyad D–A and Triad D–A1–A2 on the Efficiency of Ultrafast Intramolecular Charge Separation from the Second Excited State. *Chem. Phys.* **2016**, *478*, 164-172.

[81] Edri, E.; Aloni, S.; Frei, H. Fabrication of Core-Shell Nanotube Array for Artificial Photosynthesis Featuring an Ultrathin Composite Separation Membrane. *ACS Nano* **2018**, *12*, 533-541.

Table 1. Comparison of measured IR frequencies with gas-phase DFT-calculated harmonic frequencies (6-31++G**/ ωB97X-D; see Table S8 for full set).

	Pyridine^0		**Transient Species**		
Vib Mode Number	**Observed (cm^{-1})**	**Calculated (cm^{-1})**	**Observed (cm^{-1})**	**Anion Calculated (cm^{-1})**	**Cation Calculated (cm^{-1})**
18	1378	1367	1354	1347	1318
19	1440	1489	1410	1379	1454
20	1500	1514	1445	1443	1497
21	1653	1657	***1484***	***1497***	***1554***
22	1667	1661	**1630**	**1636**	**1655**

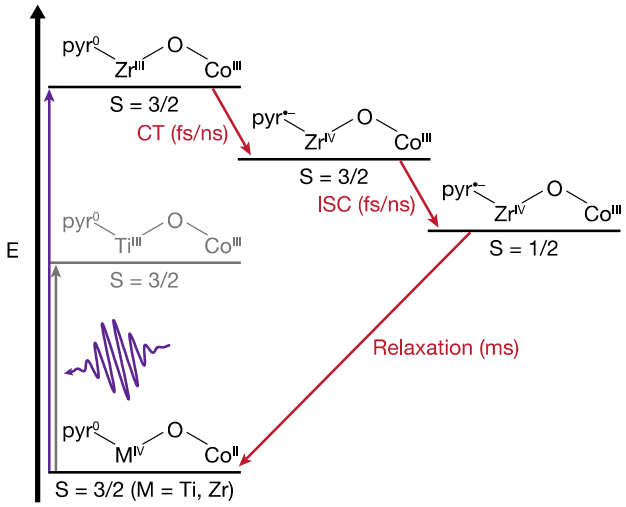

Figure 1: ZrOCo and TiOCo binuclear units absorb light to form excited MMCT states. Excited ZrOCo is capable of reducing the adjacent pyridine moiety; the system subsequently undergoes intersystem crossing to a long-lived, charge-separated state. Excited TiOCo does not have sufficient potential for electron transfer to pyridine.

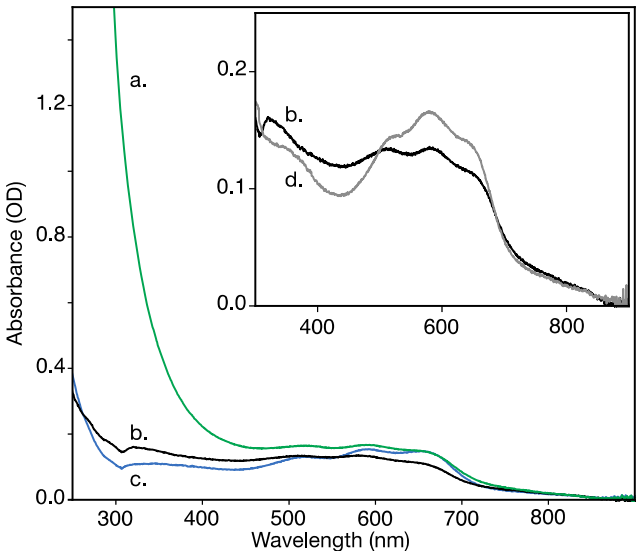

Figure 2: UV-visible spectra of heterobinuclear light absorbers on 12 nm silica nanoparticles pressed into pellet measured in transmission mode. (a) TiOCo, (b) ZrOCo, and (c) Co. Light scattering contribution by silica was subtracted, and intensities are normalized to pellet size of 20 mg. Inset shows (d) ZrOCo sample after loading with pyridine, compared with the same sample before adding pyridine (b). The small dip at 307 nm present in all spectra is an instrument artifact.

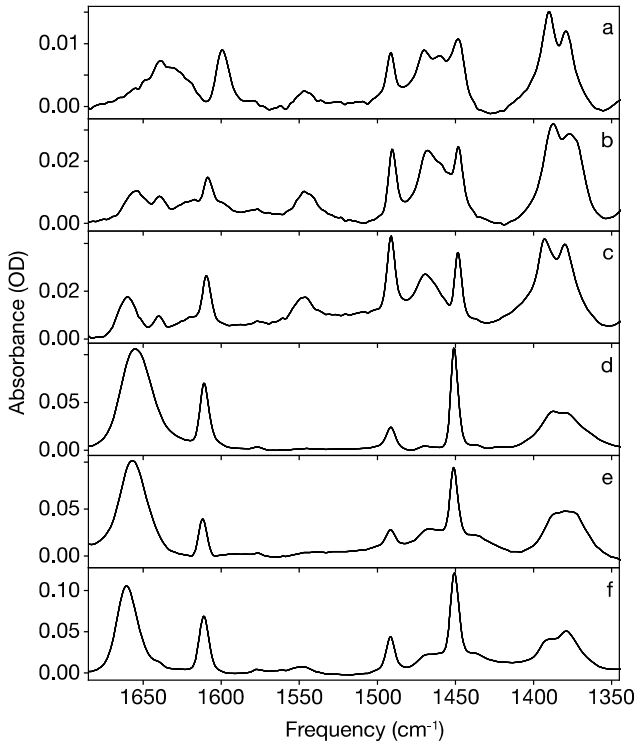

Figure 3: FT-IR spectra of pyridine loaded by solution-phase method onto (a) silica nanoparticles; (b) titanium monometallic material; (c) zirconium monometallic material; (d) cobalt monometallic material; (e) TiOCo material; (f) ZrOCo material. Note the lower intensity of spectra a, b, and c due to weaker adsorption of pyridine without cobalt present. Background peaks associated with the bending mode of surface-adsorbed water at 1643 cm^{-1} and the silica overtone mode at 1865 cm^{-1} were subtracted from all samples.

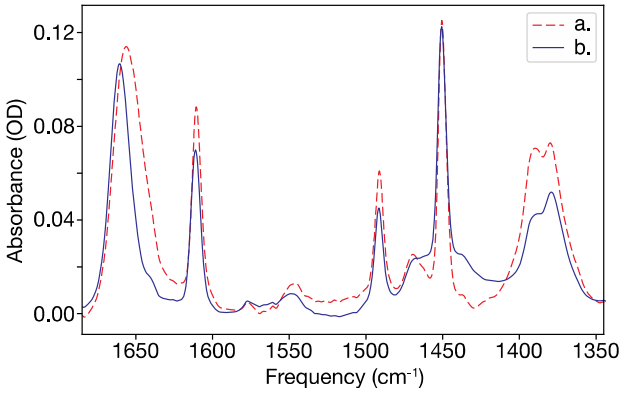

Figure 4: FT-IR spectra of (a) the sum of Zr-pyr and Co-pyr added without scaling compared with (b) ZrOCo-pyr material.

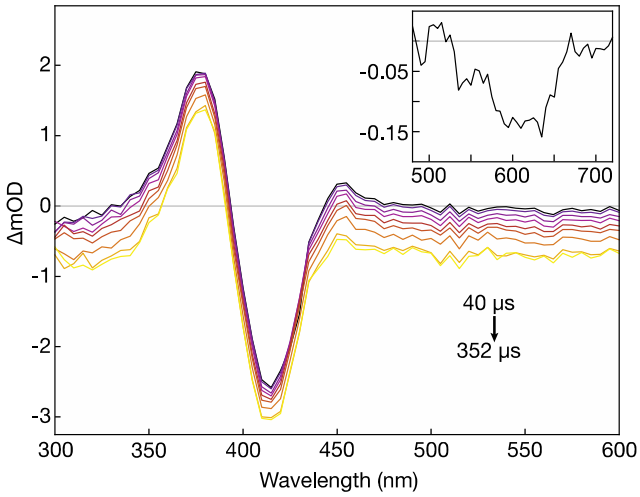

Figure 5: Transient absorption spectra of ZrOCo-pyr material following excitation at 425 nm recorded with detector in slow-response mode. Inset shows time-average bleach of d-d transition using Savitzky-Golay smoothing filter (7-point/linear). From darkest to lightest, time slices correspond to spectra at 40, 44, 52, 60, 72, 84, 112, 192, 272, and 352 µs.

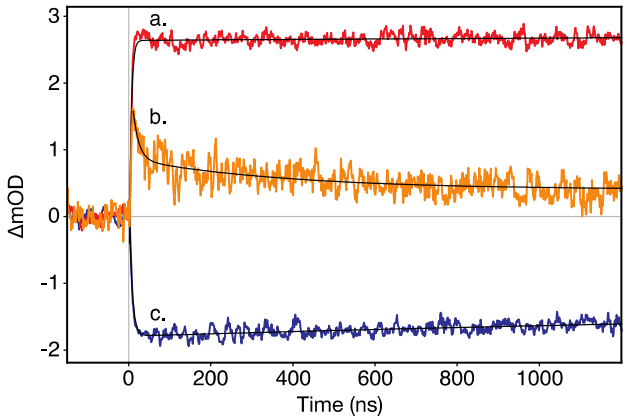

Figure 6: Transient absorption kinetics data for ZrOCo-pyr and TiOCo-pyr materials. The Zr-Co sample was measured at (a) the center of the product peak (375 nm) and (c) the nearest accessible shoulder of the bleach (400 nm, which was determined by the optical high-pass filter required for avoiding detection of scatter laser excitation light). The excited state appears within the lifetime of the laser pulse (9±1 ns) and persists into the hundreds of ms range (Figure 8). By comparison, the TiOCo-pyr sample (b) shows only the electrostriction response in the 350-400 nm regions. Trace (c) shows a modest apparent recovery caused a slight narrowing of the product peak in the overlapped pair (observed because the probe wavelength is slightly off the peak of the bleach).

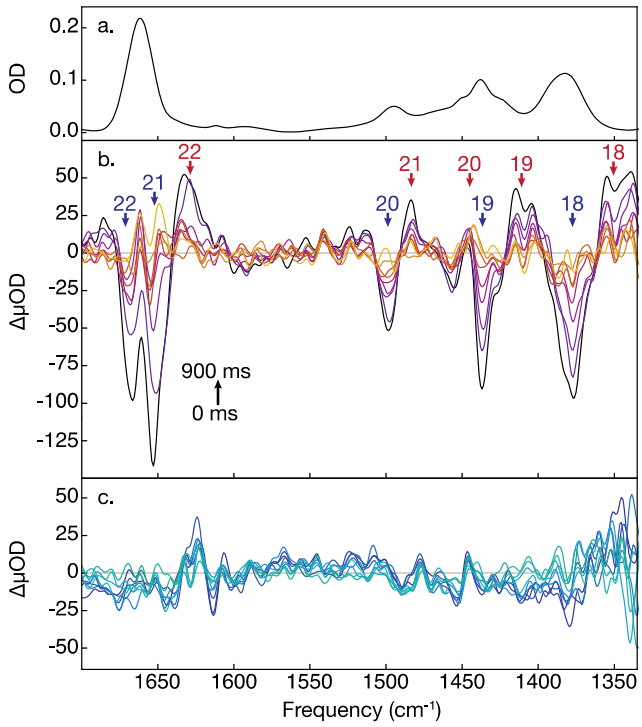

Figure 7: FT-IR spectrum ZrOCo-pyr with 0.5 mol% loading (a) and rapid-scan FT-IR spectra of ZrOCo-pyr (b) and TiOCo-pyr (c). Significant product peak formation and bleaching, consistent with the formation of pyridine radical anion, occur only for ZrOCo-pyr. From darkest to lightest, time slices correspond to 0, 60, 180, 300, 420, 540, 660, 780, and 900 ms. All peaks return to baseline within 1 ms. Shifts in the silica and water background due to refractive index changes from slight heating due to the 120 ms excitation were subtracted from each spectrum: the dominant silica baseline shift was removed by subtracting a third-order polynomial fit over the region from 1330 to 1770 cm^{-1}, while the less significant water-associated baseline shift was the only feature remaining in the RS-FT-IR spectra of Co-pyr (Figure S5). This feature was modeled with two Gaussian profiles, and subtracted from spectra of ZrOCo-pyr and TiOCo-pyr, leaving only changes associated with pyridine.

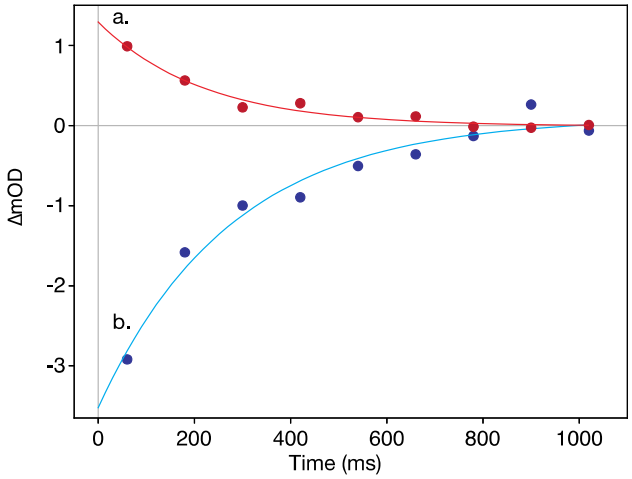

Figure 8: Rapid-scan FT-IR kinetics data with single-exponential fit curves for integrated product absorptions (a) and recovery of bleaches (b) for ZrOCo-pyr. The lifetime of (a) is 220 ± 60 ms and of (b) is 280 ± 60 ms.

TOC Graphics